



## To what extent are the IASI water vapour profiles representative of the conditions in the autumn before the HPE? Lessons learned from the WaLiNeAs campaign

5 Patrick Chazette<sup>1</sup>, Andreas Behrendt<sup>2</sup>, Adolfo Comerón<sup>3</sup>, Paolo Di Girolamo<sup>4</sup>, Marco Di Paolantonio<sup>4,5</sup>,  
Davide Dionisi<sup>5</sup>, Cyrille Flamant<sup>6</sup>, José Luis Gómez-Amo<sup>7</sup>, Jérémie Lagarrigue<sup>1</sup>, Frédéric Laly<sup>1,8</sup>, Diego  
Lange<sup>2</sup>, Constantino Muñoz-Porcar<sup>3</sup>, Alejandro Rodríguez-Gómez<sup>3</sup>, Michaël Sicard<sup>3,9</sup>, Donato Summa<sup>10</sup>,  
Julien Totems<sup>1</sup>, María Pilar Utrillas<sup>7</sup>, Pedro C. Valdelomar<sup>7</sup>, Volker Wulfmeyer<sup>2</sup>

<sup>1</sup>Laboratoire des Sciences du Climat et de l'Environnement (LSCE), UMR8212, Laboratoire mixte CEA-CNRS-UVSQ, CEA Saclay, 91191 Gif-sur-Yvette, France.

10 <sup>2</sup>Institut Fur Physik Und Meteorologie, Universitat Hohenheim, Stuttgart, Germany

<sup>3</sup>CommSensLab, Department of Signal Theory and Communications, Universitat Politècnica de Catalunya (UPC), Barcelona, Spain

<sup>4</sup>Dipartimento di Scienze della Salute, Universita degli Studi della Basilicata, Potenza, Italy

<sup>5</sup>Institute of Marine Sciences, National Research Council, Rome, Italy

15 <sup>6</sup>LATMOS/IPSL, CNRS-SU-UVSQ, Sorbonne Université, Paris, France

<sup>7</sup>Solar Radiation Group, Departament de Física de la Terra i Termodinàmica, Universitat de València, Spain

<sup>8</sup>ADDAIR Company, 78530, Buc, France

<sup>9</sup>LACy, Laboratoire de l'Atmosphère et des Cyclones UMR 8105 CNRS, Université de La Réunion, Météo-France, Saint-Denis, Réunion, France

20 <sup>10</sup>Institute of Methodologies for Environmental Analysis, National Research Council, Tito Scalo, Italy

*Correspondence to:* Patrick Chazette (Patrick.chazette@lsce.ipsl.fr)

Keywords: Raman, Lidar, IASI, ERA5, Water vapour, WaLiNeAs

**Abstract.** The WaLiNeAs campaign took place along the north-western Mediterranean coast between October 25 2022 and January 2023. This period was marked by unusual weather conditions associated with dry autumn and winter. In such conditions and for the first time, eight ground-based stations equipped with water vapour Raman lidars were strategically deployed by four European countries. We studied the consistency of this network with the water vapour mixing ratio (WVMR) products derived from the Infrared Atmospheric Sounding Interferometer (IASI) and the European Centre for Medium-Range Weather Forecasts (ECMWF) Reanalysis (ERA5), which assimilate IASI radiances. The statistical metrics used in the comparison are the mean bias (MB, defined as lidar – 30 IASI or ERA5), the root mean square error (RMSE) and the correlation coefficient (COR). A positive MB of approximately  $0.9 \text{ g kg}^{-1}$  (respectively  $0.6 \text{ g kg}^{-1}$ ) between 0.2 and 5 km above mean sea level (amsl) indicates a systematic underestimation of the WVMR by IASI (respectively ERA5). RMSE values range from 1 to  $2 \text{ g kg}^{-1}$  across all lidar stations for IASI and ERA5, while the measurement uncertainties of the lidars are typically below 0.4  $\text{g kg}^{-1}$ . COR presents little variation between stations, it ranges from 0.7 to 0.8 and remains almost constant 35 between 0.2 and 5 km amsl. Both the IASI and the ERA5 products appear to accurately reproduce the temporal variability of the vertical structure of water vapour in the low troposphere. Nevertheless, they show MB and RMSE significantly above the uncertainties of lidar measurements.

### 1 Introduction

The Infrared Atmospheric Sounding Interferometer (IASI) has been on board the polar-orbiting MetOp (Meteorological 40 Operational) meteorological satellites since 19 October 2006. These satellites form the space segment of the Exploitation of Meteorological Satellites (EUMETSAT) Polar System (EPS). Three generations of the IASI instrument (A to C) have been launched, with the latest being launched on 7 November 2018 and are still operational. This article uses data from the latest generation. The main mission of IASI is operational meteorology (Zhou et al., 2009). The infrared spectra measured by IASI are used directly in variational assimilation for weather forecasting (Hilton et al., 2009, 2012b; Xu et al., 2013; Matricardi and



45 McNally, 2014; Heilliette et al., 2013). Alongside the assimilation of radiances, vertical profiles of water vapour mixing ratios (WVMR) are derived directly from infrared radiances on a global scale (Carissimo et al., 2005; Schlüssel et al., 2005; Schneider et al., 2010; Amato et al., 2009). The vertical distribution of WVMR is obtained using spectral intervals that are selected to ensure their weight functions are homogeneously distributed in the atmosphere.

Although the Level-2 water vapour product of IASI has received little validation, it could play a key role in improving our 50 understanding of frontogenesis, convection (Held and Soden, 2000), cloud formation and aerosol hydration (Rood et al., 1987; Randriamiarisoa et al., 2006). Indeed, atmospheric water vapour acts as an energy reservoir, exchanging energy with both the atmosphere and the surface via condensation and evaporation processes involving latent heat flux. These processes all play an important role in the current context of climate change (IPCC, 2022). While the literature describes some validation exercises 55 using radiosondes (Pougatchev et al., 2009), other authors present lidar as an excellent candidate for validating IASI water vapour products (Masiello et al., 2013). However, these comparisons were performed using only six lidar profiles. The most recent work on validating IASI-derived WVMR vertical profiles was conducted over the Mediterranean as part of the international Hydrological Cycle in the Mediterranean eXperiment (HyMeX) and Chemistry-Aerosol Mediterranean Experiment (ChArMEx) programmes (Chazette et al., 2014a). Raman lidar measurements were taken on the island of Menorca (Balearic Islands, Spain). A total of around 30 coincidences were obtained during autumn 2012 for HyMeX and summer 2013 60 for ChArMEx. While this work was more statistically representative, it did not incorporate the spatial variability of water vapour or assess biases. Furthermore, significant biases were revealed through comparisons between the European Centre for Medium-Range Weather Forecasts (ECMWF) Reanalysis (ERA5) (<https://cds.climate.copernicus.eu/>, last access: 13 August 2025), which assimilates IASI radiances (Hersbach et al., 2020), and vertical lidar profiles (Laly and Chazette, 2025). These 65 biases could exceed  $2 \text{ g kg}^{-1}$  in the first three kilometres of the atmosphere and, under heatwave conditions,  $\sim 3 \text{ g kg}^{-1}$  in the free troposphere. The biases must be corrected before any IASI data can be used in weather forecasts. The same applies to the future assimilations of lidar measurements (Hilton et al., 2012b; Fourrié et al., 2019). It should be noted that current knowledge suggests that lidar and IASI measurements could complement each other, with lidar compensating for IASI's lack of lower-layer sampling.

The WAtter Vapor LiDAR NEtwork Assimilation (WaLiNeAs) project (Flamant et al., 2021) provides an opportunity to improve 70 the knowledge on the complementarity between the IASI- and lidar-derived WVMR profiles in the low troposphere. The field campaign, which took place from October 2022 to January 2023, was conducted across the coastal north-western Mediterranean area. It was used to compile an unparalleled database (Laly et al., 2024) of vertical WVMR profiles at eight sites equipped with Raman lidar. These sites were located between Valencia (Spain, westernmost site) and Ajaccio (Corsica, France, easternmost) to sample the upstream conditions of extreme precipitation phenomena initiated by the advection towards 75 the coast of low-level flows heavily laden with moisture during the autumn period (Ricard et al., 2012). This article aims to analyse the statistical coherence between the WVMR Level-2 products derived from IASI on board METOP-C and the Raman lidar involved during WaLiNeAs. It includes complementary analyses with ERA5 which uses IASI radiances in its assimilation scheme.

Section 2 describes the various Raman lidars used and the ground-based stations, while Section 3 gives an overview of IASI 80 and ERA5. The method used to compare the lidar data with the IASI and ERA5 operational products is presented in Section 4. Section 5 presents and discusses the statistical results. The conclusion is given in Section 6.

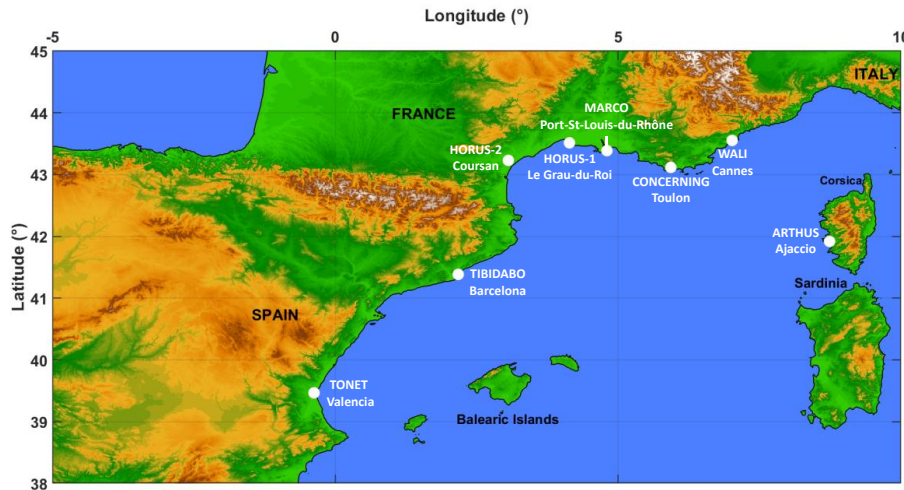
## 2        **WaLiNeAs field experiment**

### 2.1      **Site and lidar descriptions**



85 The comparison between the WVMR ground-based lidar measurements and the IASI operational products took place in the frame of WaLiNeAs between October 2022 and January 2023. The WVMR vertical profiles derived from the IASI spaceborne spectrometer were compared with those measured by eight Raman lidars located along the western Mediterranean coast of Europe as shown in Figure 1. Table 1 shows the geographical location of each site and their identification number used throughout the article. The useful characteristics of the eight Raman lidars are summarised in the Appendix A alongside the calibration process for each Raman lidar.

90 The technology used for each lidar is similar, as is the data inversion procedure. Useful references are given in Table 1. The maximum uncertainty lies with the contributions of bias and standard deviation. The bias is mainly due to the lidar calibration, whereas the standard deviation is due to shot noise. For this study, we will only consider measurements with a statistical error of less than  $0.4 \text{ g kg}^{-1}$ . Biases are mainly related to calibration and remain in the order of  $0.3 \text{ g kg}^{-1}$ . The intrinsic biases of the instruments are mostly less than  $0.1 \text{ g kg}^{-1}$ .



95

**Figure 1:** Location of the eight stations (in white) of the Raman lidar network deployed during the WALINEAS field campaign.

**Table 1:** Raman lidars (RL) involved during WaLiNeAs, their locations and identifications (Id) during the project.

Raman lidar	Close location	Longitude east / Latitude north Altitude amsl	Id
TONET (ACTRIS) (New lidar)	Valencia	-0.42° / 39.5° 60 m	RL1
TIBIDABO (ACTRIS) (Kumar et al., 2011)	Barcelona	2.11° / 41.38° 115 m	RL2
HORUS-2 (Laly et al., 2024)	Coursan	3.06° / 43.23° 4 m	RL3
HORUS-1 (Laly et al., 2024)	Grau-du-Roi	4.13° / 43.52° 7 m	RL4
MARCO (Di Girolamo et al., 2023b)	Port-Saint-Louis-du-Rhône	4.81° / 43.39° 5 m	RL5
CONCERNING (Di Girolamo et al., 2023a)	Toulon	6.01° / 43.14° 65 m	RL6
WALI (Chazette et al., 2014b)	Cannes	6.96° / 43.54° 4 m	RL7
ARTHUS (Lange et al., 2019)	Ajaccio	8.85° / 41.70° 20 m	RL8

## 2.2 Spaceborne and modelling data



### 2.2.1 MetOp/IASI

IASI is a Fourier transform spectrometer on board a series of three polar heliosynchronous orbiting satellites, which were launched in 2006, 2012 and 2018, respectively. It is part of the MetOp program, which forms the space segment of the overall EUMETSAT Polar System (EPS) (Klaes et al., 2007). The orbit has a 29-day cycle, and the ground track crosses the equator at 09:30 local time. IASI operates in the spectral region between 645 and 2,760 cm<sup>-1</sup>, achieving a resolution of 0.5 cm<sup>-1</sup> after apodisation. Its ground swath width is approximately 2,200 km, providing global Earth coverage twice per day. The main objective of the spaceborne mission is to provide global-scale constraints for operational meteorology (Coopmann et al., 2020), with a second mission focused on atmospheric composition (Clerbaux et al., 1998; Cuesta et al., 2020). IASI makes a significant observational contribution to variational assimilation for weather forecasting (Hilton et al., 2009; Guidard et al., 2011). Although radiances are assimilated directly, analysis and reanalysis datasets are only generated using channels with weight functions selected above 2 km amsl, the planetary boundary layer (PBL) is therefore less directly constrained by IASI measurements.

The IASI Level-2 processing development specifically aimed to generate operational WVVMR profiles (available at <https://data.eumetsat.int/data/map/EO:EUM:DAT:METOP:IASSND02#>, last access: 20 December 2025), which are currently distributed on a 90-level grid extending between 0.005 and 1050 hPa (August et al., 2012; Schlüssel et al., 2005). The products are derived from the release 1.1 of the climate data record of "all-sky" temperature and humidity profiles and their associated quality parameters using the latest operational EUMETSAT algorithms available (V6.5.4, 12/2019) (EUMETSAT, 2022). IASI-derived WVVMRs are obtained under cloud-free conditions, with vertical resolution of 1–2 km in the lower troposphere (Hilton et al., 2012a) and horizontal resolution of 25 km x 25 km. Nevertheless, operational products are provided at around 40 levels between sea level and 5 km amsl, for vertical sampling ranging from 20 m near the surface to 250 m at 5 km amsl. To compare with lidar data, the WVVMR profiles derived from IASI were then linearly interpolated to match the vertical resolution of the lidars of 100 m. Note that for the WVVMR retrieval, the IASI weighting functions generally reach a maximum value above 700 hPa. Consequently, sensitivity to the lower troposphere is reduced, leading to greater error below 3 km, where ~80% of moisture is present. The mean relative uncertainty of the WVVMR product is given to be 10%.

### 2.2.2 ERA5

The WVVMR profiles derived from the European Centre for Medium-Range Weather Forecasts (ECMWF) Reanalysis (ERA5) (Hersbach et al., 2020) are used for pressure level above 500 hPa (<https://cds.climate.copernicus.eu/>, last access 31 August 2025). They correspond to altitudes below 5 km amsl, which are distributed over 15 levels. The vertical resolution is approximately 200 m near ground level and 700 m at 5 km amsl. The ERA5-derived WVVMR are then interpolated to match the vertical resolution of the lidar profiles. The horizontal resolution is 0.25° of longitude by 0.25° of latitude, which is approximately equivalent to 21 km by 28 km at a latitude of 40°.

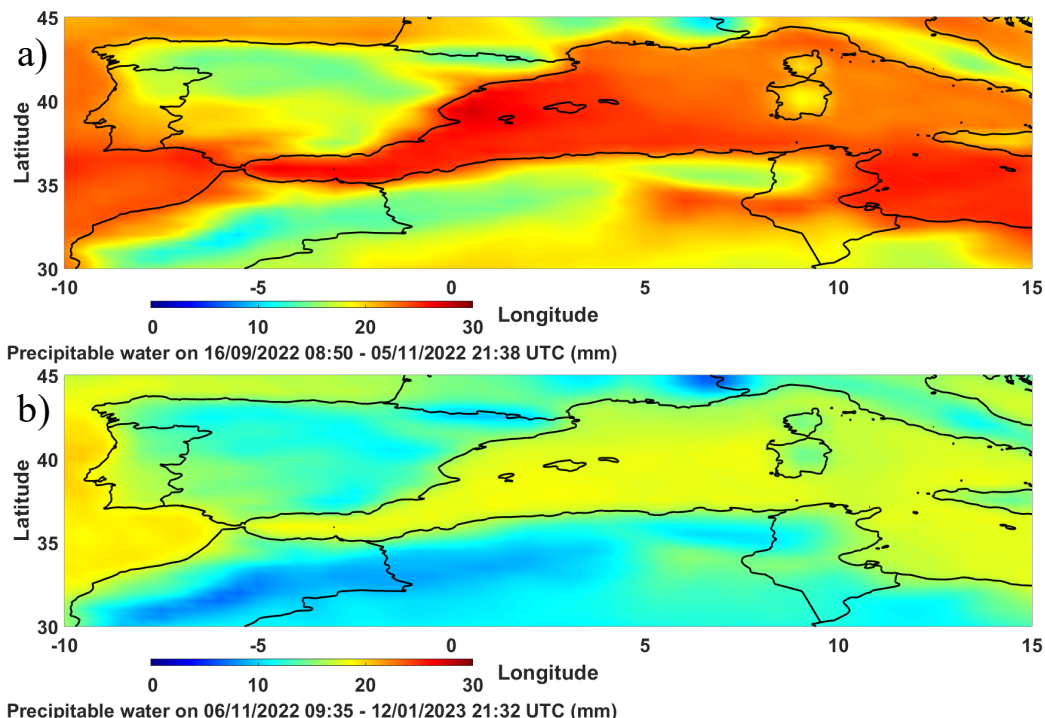
### 2.3 Meteorological context

Autumn 2022 was characterised by unusual weather conditions in the western Mediterranean basin, including persistent positive temperature anomalies and widespread rainfall deficits. This followed an exceptionally hot summer, the effects of which continued into autumn through enhanced atmosphere-ocean interactions. Indeed, temperatures were well above normal levels (~3°C), particularly in September and October. Significant positive temperature anomalies were observed over southern Europe and the western Mediterranean, reflecting the persistence of warm air masses and atmospheric blocking patterns. These conditions were reinforced by exceptionally high sea surface temperatures of the western Mediterranean Sea, resulting from heat accumulation during the summer of 2022. Compared to climatology, anomalies of several degrees (~4°C) were observed (Guinaldo et al., 2023).



Despite this thermodynamic context being favourable to instability, atmospheric circulation on a synoptic scale was dominated  
140 by recurrent anticyclonic conditions over Western Europe and the Mediterranean basin. This limited the intrusion of low-  
pressure systems and the establishment of unstable southerly flows, reducing the frequency and intensity of the Mediterranean  
weather systems typically observed in autumn (Blanchet et al., 2021). Consequently, autumn total precipitation amounts were  
significantly below normal by ~24%.

Despite the lower troposphere being drier than normal, two contrasting periods were observed. These periods are evident in  
145 the temporal syntheses derived from IASI measurements, as illustrated in Figure 2, which depicts the precipitable water content  
over the western Mediterranean basin. Figure 2a shows the wettest period, while Figure 2b shows the driest period after 5  
November 2022. The temporal evolution of lidar, spaceborne and modelling data in the supplementary material will highlight  
this. Precipitable water content is homogeneous across the western basin, but there is a significant variation between the two  
periods, with a ~30% decrease between the beginning of November and the rest of the year.



150 **Figure 2:** Precipitable water derived from IASI products during the wet period (16 September to 5 November 2022) and the dry period (6 November 2022 to 12 January 2023), as observed during the WaLiNeAs field campaign.

### 3 Data processing methods

#### 3.1 Consistency between lidar calibrations

155 The lidars were calibrated individually using radiosondes and/or ground-based weather stations using similar approaches. This  
raises the question of how to standardize these different calibration procedures. To assess this, we compared each lidar's data  
over its entire operating period with reanalyses of ERA5. ERA5 is constrained by multiple sources of vertical profiles,  
including radiosondes, the IAGOS (In-Service Aircraft for a Global Observing System) network and IASI observations above  
2–3 km (Hersbach et al., 2020). For this reason, ERA5 most closely mimics the hourly radiosonde observations that would  
160 have been available near the various lidar stations of the WaLiNeAs network. As an example, we present the comparison



between all radiosondes and ERA5 for the period November–December 2022 at the meteorological station of Nîmes (Météo-France), located 40 km north of Grau-du-Roi, in the supplementary material (Figure S1). The relationship is linear with a slope of 0.99 and an intercept of  $0.054 \text{ g kg}^{-1}$ , a strong correlation of 0.99 and a low mean bias of  $+0.02 \text{ g kg}^{-1}$ . The standard deviation is around  $0.36 \text{ g kg}^{-1}$ . Furthermore, as shown in Laly and Chazette (2025), for the sites of the Grau-du-Roi (RL4) and Cannes (RL7), the ERA5 pixels around a central pixel are strongly correlated ( $\text{COR} > 0.97$ ), and exhibit MBs with an absolute value below  $0.14 \text{ g kg}^{-1}$ .

165 For all lidars, we therefore sought a calibration yielding a slope of 1 in the comparison with ERA5. This required applying a site-specific correction factor. As shown in Table 2, the correction factors are small, ranging from -7% to 10%. This attests to the quality of the original calibrations carried out independently at each station. More or less significant biases between lidar  
170 and ERA5 remain, as shown in the Supplementary Figures S2 to S9. In some cases, these may be associated with imperfect corrections for molecular and particulate contributions in the lidar data. Nevertheless, the same process has been used to correct all lidar signals for molecular transmission, and the residual error is below  $0.02 \text{ g kg}^{-1}$ . The contribution of aerosols remains small, either because aerosol optical thicknesses (AOTs) values are below 0.15, or because the aerosols are primarily desert dust with Ångström exponents below 0.5. Although aerosol-related bias becomes more significant at higher altitudes (Chazette  
175 et al., 2014b) it remains below  $0.1 \text{ g kg}^{-1}$  in our data. Note that RL2, RL6 and RL8 use a rotational Raman channel for oxygen and nitrogen in addition to the vibro-rotational Raman channel for water vapour. Because the wavelength difference is larger in this configuration, the effect of aerosols is more pronounced. In this case, failure to correct for aerosols leads to an overestimation of the WVMR. For a typical AOT of 0.2 (at 355 nm) and an Ångström exponent of 1.5 (corresponding to pollution aerosols), the overestimation could reach approximately +4%, decreasing progressively closer to the lidar, and it is  
180 less than 1% for dust and marine aerosols.

Another potential source of bias is imperfect correction of the overlap factor in the lower layers. The minimum range of WVMR data is ensured to be below 200 m (see Table 1) because the  $\text{N}_2$ - and  $\text{H}_2\text{O}$ -Raman channels share the same optical path. The remaining divergences are mainly related to the near range due to the angular acceptance of the interference filters. Overall, biases related to the instrument itself and to the data inversion procedure remain below or on the order of  $0.1 \text{ g kg}^{-1}$   
185 for all lidars. This justifies performing only a slope correction with respect to ERA5, given the good coefficients of determination obtained (between 0.71 and 0.91).

The intercept values reported in Table 2, representing systematic biases, are the result of multiple contributions that can partially cancel each other. Nevertheless, biases with an absolute value greater than  $0.1 \text{ g kg}^{-1}$  are considered more likely attributable to modelling rather than instrument error. For this reason, such intercepts in Table 2 have not been used in the lidar  
190 calibration process.

**Table 2:** Statistical parameters of the regression between lidar and ERA5 data. The calibration correction factor must be applied to each lidar data set in order to obtain a slope of 1 for the regression line.

	RL1	RL2	RL3	RL4	RL5	RL6	RL7	RL8
Calibration correction factor (%)	+10	+2.0	0	+1.4	+6	-7	-1.5	0
Intercept ( $\text{g kg}^{-1}$ )	0.03	0.54	0.67	1.00	0.62	0.10	0.45	0.19
Coefficient of determination	0.88	0.83	0.91	0.87	0.75	0.82	0.91	0.87

195 **3.2 Statistical metrics**



Comparisons between LIDAR measurements and IASI overpasses were performed by considering the nine pixels surrounding each site (Figure 3), corresponding to an area of 75 km x 75 km. Because the stations are located near the coastline, at least one of these pixels always provides information on the lower troposphere. The lidar data were averaged over a one-hour period, using profiles within  $\pm 30$  minutes of the satellite overpass time. The signal-to-noise ratio is significantly improved by this averaging, with uncertainties of less than 0.4 g kg<sup>-1</sup> being achieved in the low troposphere. The number of IASI pixels contributing to the comparison varies with altitude, as the surrounding topography must be taken into account. Within the perimeter defined by the nine pixels, the local summits generally remain below 500 m amsl, ensuring minimal terrain obstruction.

The statistical indicators used to evaluate the consistency of the IASI-derived WVMR ( $r_{iasi}$ ) with respect to lidar measurements ( $r_{lidar}$ ) are the mean bias (MB), the root mean square difference (RMSD), the root mean square error (RMSE) and the (Pearson) correlation (COR). These metrics are commonly used to assess model performance (Boylan and Russell, 2006; Tombette et al., 2008) and given for each altitude  $z$  by:

$$MB(z) = \langle r_{lidar}(t, z) \rangle - \langle r_{iasi}(t, z) \rangle \quad (1)$$

$$RMSD(z) = \sqrt{\langle (r_{lidar}(t, z) - r_{iasi}(t, z))^2 \rangle} \quad (2)$$

$$RMSE(z) = \sqrt{RMSD^2 - MB^2} \quad (3)$$

$$COR(z) = \frac{\langle (r_{lidar}(t, z) - \langle r_{lidar}(t, z) \rangle) \cdot (r_{iasi}(t, z) - \langle r_{iasi}(t, z) \rangle) \rangle}{\sqrt{\langle (r_{lidar}(t, z) - \langle r_{lidar}(t, z) \rangle)^2 \rangle} \cdot \sqrt{\langle (r_{iasi}(t, z) - \langle r_{iasi}(t, z) \rangle)^2 \rangle}} \quad (4)$$

where  $\langle \rangle$  is the temporal averaging. The altitude averaged MB ( $\widetilde{MB}$ ) and RMSE ( $\widetilde{RMSE}$ ) are then derived using the relationships:

$$\begin{aligned} \widetilde{MB} &= \frac{1}{(z_b - z_a)} \cdot \int_{z_a}^{z_b} MB(z) \cdot dz \\ \widetilde{RMSE} &= \sqrt{\frac{1}{(z_b - z_a)} \cdot \int_{z_a}^{z_b} RMSD(z)^2 \cdot dz - \widetilde{MB}^2} \end{aligned} \quad (5)$$

with the lower and upper altitudes denoted by  $z_a$  and  $z_b$ , respectively.

The CORs from different altitudes are combined using the Fisher  $\mathcal{F}$  transformation (Fouladi and Steiger, 2008). This gives the following equation for each altitude  $z$ :

$$\mathcal{F}(z) = \frac{1}{2} \cdot \log \left( \frac{1 + COR(z)}{1 - COR(z)} \right) \quad (6)$$

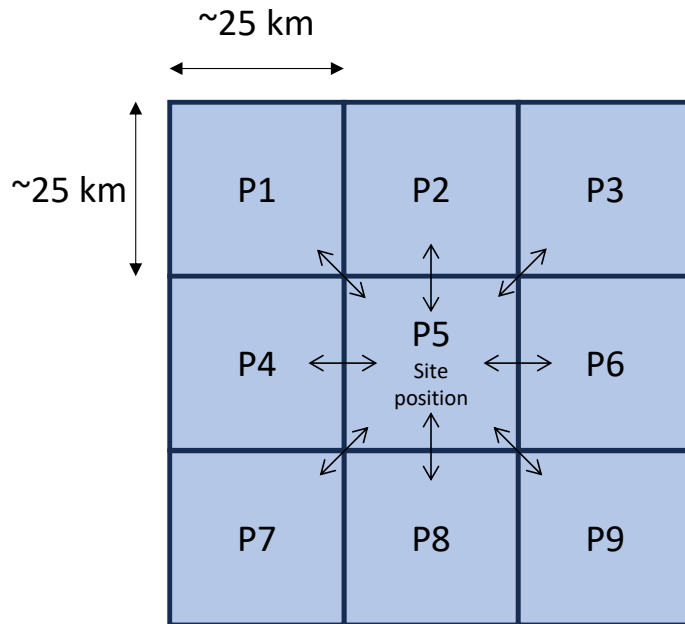
which leads to the COR averaged on the altitudes ( $\widetilde{COR}$ ) expressed by:

$$\widetilde{COR} = \frac{e^{2 \cdot \mathcal{F}} - 1}{e^{2 \cdot \mathcal{F}} + 1} \quad (7)$$

$$\text{with } \mathcal{F} = \frac{\int_{z_a}^{z_b} (N(z) - 3) \cdot \mathcal{F}(z) \cdot dz}{\int_{z_a}^{z_b} (N(z) - 3) \cdot dz},$$



where  $N(z)$  represents the number of coincidences between LIDAR and IASI at altitude  $z$ .



220 **Figure 3:** IASI pixels selected for comparison with lidar measurements. The central pixel includes the location of the lidar site. The horizontal resolution is 25 km x 25 km for the water vapour product.

#### 4 Results

The temporal evolution of the WVVMR vertical profiles corresponding to lidar measurements and coincident IASI overpasses is presented in the supplementary material. (Figures S10 to S17). Profiles derived from ERA5 are also provided. As the lidars 225 did not operate during the same periods, the temporal dynamics differ between stations. The wettest period occurs before 5 November 2022, after which the dry period begins. This transition takes place slightly later in Corsica due to the island's susceptibility to southerly winds from North Africa. Low clouds can easily be identified by the altitude range of the lidar measurements. However, there was much less precipitation than average for this region, with only one 100 mm daily precipitation event observed in Corsica around 13 November 2022. Hence, the number of coincidences with IASI varies as a 230 function of altitude, as shown by the vertical profiles of MB, RMSE and COR presented in the supplement (Figures S18 to S25). The number of samples decreases as altitude increases. This is due to the limited range of Raman lidars during daytime and under thick cloud cover.

##### 4.1 Statistical results

Table 3 summarises the statistical analysis for: i) the PBL (0.2–1.5 km amsl), ii) the transition to the free troposphere (1.5–3 km amsl), iii) the free troposphere (3–5 km amsl), and iv) all three layers combined. It is worth noting that the altitude of the top of the PBL changes over time. The first two layers in Table 3 may therefore include air mass recirculation associated with the sea-land breeze cycle and circulations that are very specific to the measurement site.

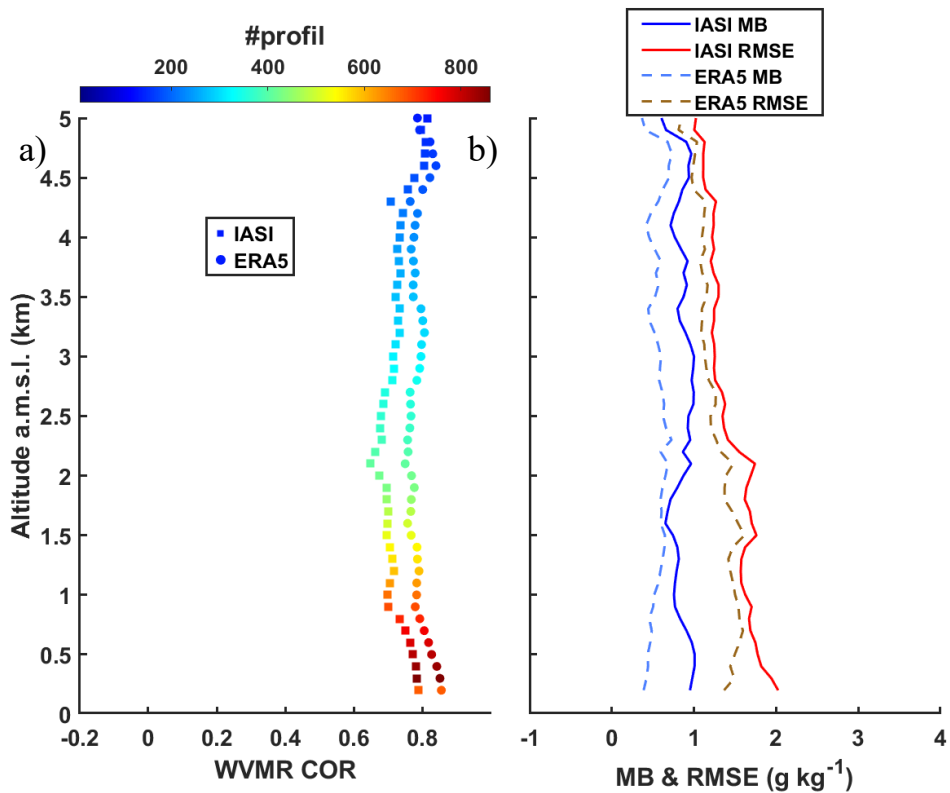
A synthesis of the behaviour of all lidars has been obtained by combining statistical profiles obtained from individual lidar systems (see Eq. 5 and 7). The vertical profiles of the three statistical parameters, following synthesis across all lidar stations, 240 demonstrate fairly consistent continuity between previous adjacent layers, highlighting that the variability of the PBL height has on average a moderate influence, albeit more noticeable at individual sites.



In general, there is a significant correlation between lidar and IASI measurements, mainly ranging from 0.7 to 0.8 (Figure 4a). This strong correlation is also evident between lidar measurements and ERA5 reanalyses. However, at the Barcelona (RL2) and Coursan (RL3) sites weaker correlations are observed (between ~0.5 and 0.7). For Coursan, the reduced correlations are 245 less significant, given the much lower number of coincidences and the reduced range of the lidar, mainly due to frequent cloud cover. The slightly lower correlations values determined for Barcelona (RL2) can be possibly explained by the location of this lidar station. It is located in an urban environment at the foothill of a 500-meter-high mountain range, and 5 kilometres from the sea. Pérez et al. (2004) have shown that, in such conditions, the atmospheric vertical structures are complex, making comparisons with reference profiles (e.g., radiosondes) problematic. In most cases, the correlations between lidar and ERA5 250 are slightly higher than those between lidars and IASI for all layers. This is due both to ERA5 assimilating additional observational datasets beyond IASI and to the lower sensitivity of IASI within the PBL. Nevertheless, WVVMR profiles derived from IASI properly represent atmospheric variability occurring from one satellite overpass to another.

The RMSEs values are fairly consistent when comparing the different lidars and remain mostly between 1 and 2 g kg<sup>-1</sup>, regardless of the layer considered (Table 3). It should be remembered that only lidar data with a statistical error of less than 255 0.4 g kg<sup>-1</sup> were considered in this study. The RMSEs shown in both Table 3 and Figure 4b are significantly higher and reflect the statistical variability between the lidar and IASI measurements. These values provide a clear indication of the uncertainty in the vertical WVVMR profiles derived from IASI in the first 5 km of the atmosphere, where most of the water vapour is present.

Interpreting biases is more difficult due to their diverse origins which are not always identifiable. As mentioned above, biases 260 related to lidar measurements are mainly associated with the reference used for calibration. The lidars were calibrated individually using in situ measurements (e.g. weather stations or radiosondes) and then recalibrated by comparing them with ERA5 data for each site. The residual biases relative to ERA5 are presented in Table 3, and the corresponding profiles are provided in the supplementary material (Figures S18b to S25b). Overall, the bias values relative to both ERA5 and IASI are similar, although slightly higher for IASI. The difference is on the order of 0.3 g kg<sup>-1</sup>. The vast majority of biases (lidar–IASI 265 or lidar–ERA5) are positive (see Figure 4b), indicating a consistent IASI underestimation of the water vapour content by +0.8–+0.9 g kg<sup>-1</sup>.



270 **Figure 4:** Synthesis of the statistical coefficients across all lidar stations when comparing lidar measurements with IASI and ERA5 products: the vertical profiles show: a) the correlation coefficient (COR); b) the mean bias (MB, lidar - IASI and lidar - ERA5) and the root mean square error (RMSE). The synthesis profiles have been obtained by combining statistical profiles derived from individual lidar systems.

**Table 3:** Statistical results (mean bias MB, root mean square error RMSE and correlation COR) synthesized from the comparisons between lidar measurements and i) IASI measurements (Bold) and ii) ERA5 reanalysis (Italic). Plain text denotes instances where the statistic is considered not representative due to insufficient data or range limitations. The number of samples for each site is shown in the supplementary material (see Figures S18 to S25).

Altitude range (km amsl)	RL1	RL2	RL3	RL4	RL5	RL6	RL7	RL8	All
MB (lidar- <b>IASI</b> or <i>ERA5</i> ) ( $\text{g kg}^{-1}$ )									
[0.2 5]	-	<b>+0.92</b> +0.49	+1.52 +0.95	+1.49 +1.37	+0.94 +0.70	<b>+0.18</b> -0.02	<b>+0.76</b> +0.53	<b>+0.44</b> +0.24	<b>+0.86</b> +0.56
]0.2 1.5]	<b>+0.79</b> +0.18	<b>+1.23</b> +0.59	<b>+1.62</b> +0.89	<b>+0.99</b> +0.99	<b>+0.72</b> +0.54	<b>+0.44</b> +0.20	<b>+0.61</b> +0.52	<b>+0.69</b> +0.32	<b>+0.86</b> +0.51
]1.5 3]	-	<b>+0.90</b> +0.52	+1.49 +1.09	<b>+1.35</b> +1.22	<b>+1.30</b> +1.07	+0.17 +0.02	<b>+0.82</b> +0.50	<b>+0.40</b> +0.35	<b>+0.89</b> +0.62
]3 5]	-	<b>+0.74</b> +0.39	+1.48 +0.89	+1.96 +1.75	+0.75 +0.42	<b>+0.01</b> -0.19	<b>+0.83</b> +0.56	<b>+0.31</b> +0.10	<b>+0.84</b> +0.54
RMSE ( $\text{g kg}^{-1}$ )									
[0.2 5]	-	<b>1.58</b> 1.47	1.53 1.38	1.36 1.02	1.64 1.43	<b>1.28</b> 1.24	<b>1.13</b> 0.97	<b>1.25</b> 1.12	<b>1.46</b> 1.28
]0.2 1.5]	<b>1.72</b> 1.26	<b>1.95</b> 1.78	<b>1.71</b> 1.74	<b>1.52</b> 1.02	<b>1.90</b> 1.53	<b>1.67</b> 1.67	<b>1.35</b> 1.10	<b>1.66</b> 1.55	<b>1.73</b> 1.50
]1.5 3]		<b>1.79</b> 1.83	1.56 1.34	1.42 1.01	<b>1.54</b> 1.38	<b>1.27</b> 1.14	<b>1.20</b> 1.06	<b>1.36</b> 1.20	<b>1.50</b> 1.31



[3 5]	-	<b>1.02</b> 0.79	1.37 1.11	0.97 0.90	1.36 1.28	<b>0.92</b> 0.92	<b>0.88</b> 0.79	<b>0.72</b> 0.60	<b>1.20</b> 1.07
<b>COR</b>									
[0.2 5]	-	<b>0.62</b> 0.69	0.55 0.64	0.78 0.89	0.66 0.77	<b>0.72</b> 0.73	<b>0.82</b> 0.86	<b>0.73</b> 0.79	<b>0.73</b> 0.80
[0.2 1.5]	<b>0.64</b> 0.82	<b>0.69</b> 0.76	<b>0.52</b> 0.63	<b>0.82</b> 0.92	<b>0.69</b> 0.81	<b>0.76</b> 0.76	<b>0.82</b> 0.87	<b>0.70</b> 0.76	<b>0.74</b> 0.81
[1.5 3]	-	<b>0.52</b> 0.49	0.48 0.57	<b>0.70</b> 0.87	<b>0.67</b> 0.76	<b>0.72</b> 0.75	<b>0.79</b> 0.84	<b>0.68</b> 0.76	<b>0.69</b> 0.77
[3 5]	-	<b>0.58</b> 0.73	0.67 0.74	0.79 0.83	0.57 0.66	<b>0.61</b> 0.59	<b>0.84</b> 0.85	<b>0.81</b> 0.87	<b>0.75</b> 0.79

275

#### 4.2 Discussion

Few comparative studies in the literature exist between IASI and lidar measurements, and the same is true for comparisons between ERA5 reanalyses and lidar measurements. Following the ChArMEx and HyMeX programmes, Chazette et al. (2014a) compared WVVMR measurements derived from the WALI lidar, which was located in the Balearic island of Menorca (Spain), 280 with IASI measurements following nighttime overpasses by METOP-A. The RMSE calculated for September–October 2012 was  $\sim 1.06$  g kg $^{-1}$  between 0 and 5 km amsl, which is consistent with the results presented in Table 3. The MB was around 0.5 g kg $^{-1}$ , slightly lower than the value found in this study, while the COR of  $\sim 0.66$  was also lower. A key difference lies in the fact that the lidar measurements from Menorca were acquired over open sea and included heavy precipitation events (HPEs), whereas the WaLiNeAs measurements were taken at coastal sites and were not affected by HPEs. A mutual bias value 285 of 0.26 g kg $^{-1}$  was reported by De Rosa et al. (2020) when comparing the Raman lidar BASIL and IASI in the altitude interval 2–15 km (RMSE = 0.30 g kg $^{-1}$ ). More recently, Laly and Chazette (2025) investigated the potential impact of atmospheric water vapour Raman lidar measurements by comparing them with WVVMR vertical profiles obtained from ERA5 data. This work was also carried out as part of the WaLiNeAs project and included the Grau-du-Roi (RL4) and Cannes (RL7) sites during 290 the dry period. In the first 5 kilometres of the atmosphere, they found an RMSE of 1.05 g kg $^{-1}$  for the Cannes (RL7) site, which is comparable to the results in Table 3 (0.97 g kg $^{-1}$ ). For this site, the MB also remained fairly close, with a value of 0.73 g kg $^{-1}$  compared to 0.53 g kg $^{-1}$ . The COR correlations are also similar (0.89 compared to 0.86). At the Grau-du-Roi site (RL4), the RMSE was slightly higher, at 1.57 g kg $^{-1}$  compared to 1.02 g kg $^{-1}$  in this study. However, the MB and COR were comparable, with values being 1.27 g kg $^{-1}$  and 0.86, respectively.

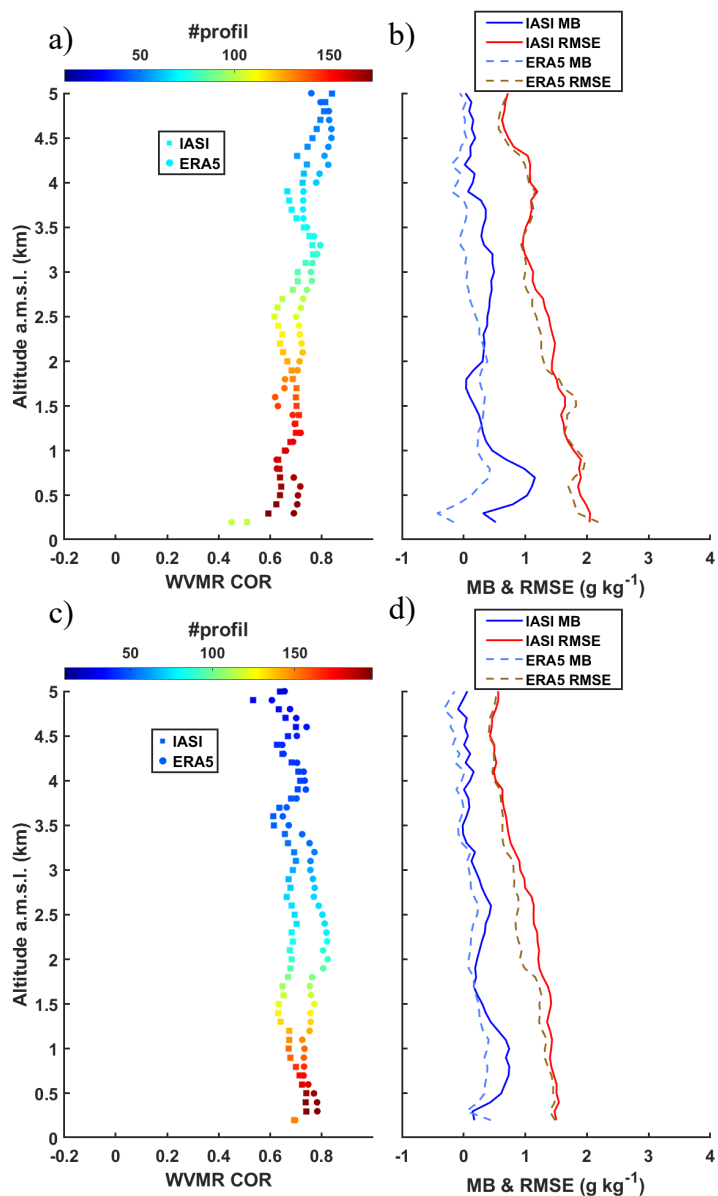
Based on the study presented here, larger dispersion of results might have been expected for the two stations (RL3 and RL4) 295 located in the Rhône Valley. In the Rhône Valley, there is often a process of recirculation, whereby the Mistral wind blows in altitude and the sea breeze blows lower down. The latter can penetrate more than 100 km inland. In addition, the lower layers in the Camargue can be very humid due to the abundance of liquid water areas. There is also a steep humidity gradient between the Mediterranean coast and inland areas, associated with various local phenomena linked to the Rhône delta's specific topography. Nevertheless, the statistical results presented here show that the temporal variability of WVVMR over the first five 300 kilometres is accurately represented by both IASI measurements and ERA5 reanalyses.

As previously explained, during the WaLiNeAs field campaign, there was a wetter period in October, followed by an exceptionally dry period from early November onwards. Most of the measurements were taken during the drier period. The 305 wetter period was less sampled, except in Barcelona (RL2), Toulon (RL6) and Ajaccio (RL8). At the Barcelona station (Figure S11), more than two-thirds of the measurements were taken during the wetter period, which may be subjected to greater variability than the drier period. This may also explain the slightly weaker correlations observed for this station (Table 3 and Figure S19a) in addition to its specific location. Note that it is more difficult to draw conclusions about the samples in the free troposphere, as there are fewer of them during the wetter period when there was heavy cloud cover. In the cases of the Toulon



(Figure S15) and Ajaccio (Figure S17) stations, however, no major differences were noted between the two time periods as shown in Table 4: and Figure 5. Slightly lower correlations are observed for the wet period in the lower layers below 3 km amsl. The trend then reverses between 3 and 5 km amsl. While there are no significant variations in the MB, the RMSE is consistently lower in dry conditions.

It is interesting to note that METOP/IASI overpasses the western Mediterranean twice a day, at 08:00–10:00 and 19:00–21:00 local time. The second time slot corresponds to nighttime conditions at the beginning of the night during the field campaign period. However, it is still early enough in the night for the PBL height to change significantly, particularly near the coast. Therefore, no notable differences were observed between the two time slots, apart from a decrease in samples and statistical representativeness when the two slots are split.





320

**Figure 5 :** Synthesis of the statistical coefficients for the Toulon (a and b) and Ajaccio (c and d) lidar stations (RL6 and RL8) when comparing lidar measurements with IASI and ERA5 products: the vertical profiles show: a) and c) the correlation coefficient (COR); b) and d) the mean bias (MB, lidar - IASI and lidar - ERA5) and the root mean square error (RMSE).

**Table 4:** Statistical results (mean bias MB, root mean square error RMSE and correlation COR) synthesized from the comparisons between lidar measurements and i) IASI measurements (Bold) and ii) ERA5 reanalysis (Italic) for RL6 and RL8. The number of samples for each site is shown in Figure 5.

Altitude range (km amsl)	[0.2 5]	[0.2 1.5]	]1.5 3]	]3 5]
Wet period				
<b>MB</b>	+0.35 +0.11	+0.60 +0.17	+0.31 +0.22	0.21 -0.03
<b>RMSE</b>	1.41 1.35	1.86 1.83	1.40 1.29	0.96 0.92
<b>COR</b>	0.68 0.72	0.65 0.68	0.67 0.71	0.75 0.79
Dry period				
<b>MB</b>	+0.26 +0.10	+0.52 +0.31	+0.28 +0.14	+0.05 -0.09
<b>RMSE</b>	1.11 0.99	1.46 1.36	1.18 0.96	0.62 0.57
<b>COR</b>	0.69 0.76	0.70 0.75	0.68 0.79	0.67 0.71

325

## 5 Conclusion

During the WaLiNeAs field campaign, eight lidar stations, evenly distributed along the Spanish and French coasts of the western Mediterranean, collected a unique set of vertical water-vapour profiles. This dataset, acquired during the exceptionally dry autumn and winter of 2022-2023, aims to assess the value of lidar measurements in the data assimilation process for weather forecasting models. For this purpose, the lidar data were compared with one of the main observational constraints of meteorological models: the European IASI instrument carried on board the METOP satellite series. For completeness, comparisons were also performed with the ERA5 reanalyses provided by ECMWF, which assimilate IASI radiances.

330

Lidar measurements mainly provide valuable information in the lower troposphere, which is poorly sampled by IASI, particularly below 3 km. Nevertheless, we show that IASI observations correlate well with the lidar measurements from the WaLiNeAs stations, with correlation coefficients generally exceeding 0.7 within the first 5 km of the atmosphere. The RMSEs quantifying the deviation between lidar and IASI measurements are relatively high, ranging from 1 to 2 g kg<sup>-1</sup>, whereas the standard deviation of the considered lidar measurements considered is less than 0.4 g kg<sup>-1</sup>. A systematic underestimation of the WVVMR profiles derived from IASI is also observed at all stations, with an average bias of +0.8 to +0.9 g kg<sup>-1</sup>. A similar but smaller underestimation is found in ERA5, typically 0.6 g kg<sup>-1</sup>. This study provided an opportunity to demonstrate the high degree of consistency between the various research lidars, despite having been developed independently by different teams from four countries in Europe. It also demonstrates that lidar measurements can provide additional relevant information for weather forecasting.

340

The IASI-NG instrument, launched on 12 August 2025, offers 30% more data on water vapour profiles with an improvement in spectral resolution compared with the version used in our study (0.25 cm<sup>-1</sup> for 0.5 cm<sup>-1</sup>, <https://user.eumetsat.int/resources/user-guides/metop-sg-iasi-ng-l1c-and-l1d-data-guide>, last access 26 November 2025). This increase in spectral resolution is accompanied by an increase in vertical resolution. IASI-NG measurements should therefore enable a more accurate characterization of water vapour in the low troposphere. Using a similar lidar framework as in WaLiNeAs would be of particular interest, as lidars appear to provide both a relevant validation tool and a valuable complement to spaceborne measurements.



## Appendix A: Lidar descriptions

350 This appendix outlines the key features of Raman lidars and sites. Table A1 summarises the lidar characteristics.

**Table A1:** Characteristics of the water vapor Raman lidar used during the WaLiNeAs field campaign. The uncertainties are given for an average profile calculated over a period of one hour.

	RL1	RL2	RL3	RL4	RL5	RL6	RL7	RL8	
<b>Emitted wavelength (nm)</b>	~354.7								
<b>Reception channels (nm)</b>	387.5 407.5	353.9 407.5		387.5 407.5					
<b>Energy (mJ)</b>	80	90	30	30	0.25	110	100	100	
<b>Repetition rate (Hz)</b>	20	20	100	20	20000	100	20	200	
<b>Telescope diameter (cm)</b>	30	38	15	15	40	50	15	40	
<b>Telescope field-of-view (mrad)</b>	2.1	2	1.6	1.6	0.31	0.55	1.6	0.6	
<b>Laser divergence (mrad)</b>	0.7	0.5	0.2	0.2	0.3	0.39	0.2	0.4	
<b>Power-aperture product (W m<sup>2</sup>)</b>	0.11	0.20	0.053	0.011	0.63	2.16	0.035	2.5	
<b>Native vertical resolution (m)</b>	7.5	3.75	0.75	0.75	15	7.5	0.75	7.5	
<b>Final vertical resolution (m)</b>	100								
<b>Maximum daytime range (km)</b>	-	1.5	2	1.5	2	3-4	2	4	
<b>Maximum nighttime range (km)</b>	4.5	6	8	7	5	6	10	12	
<b>Minimum range of WVMR data (m)</b>	200	90	150	150	100	100	150	200	
<b>Native time resolution (min)</b>	1	1	1	1	0.05	0.17	1	0.17	
<b>Final time resolution (min)</b>	30								

### TONET at Valencia (RL1)

355 TONET Lidar is deployed at Burjassot Atmospheric meaSurement Station (BASS, 39.5 °N, -0.42 W, 60 m amsl). It is an Aerosol Remote Sensing (ARS) site of the Aerosol, Clouds and Trace Gases Research Infrastructure (ACTRIS) located in the metropolitan area of Valencia city, 10 km distant to the Mediterranean Sea. TONET Lidar is 8-channel Raman depolarization Lidar (LR332-D300) manufactured by Raymetrics S.A. The instrument is equipped with a Nd:YAG pulsed laser beam emitting 80 mJ at 355 nm pointed vertically upward. The receiver is based on a 30 cm Cassegrain optical telescope design. Two Raman detection channels were used for the field-campaign: one for nitrogen (387.5 nm) and the other for water vapour (407.5 nm). The backscattered signal is detected using photomultiplier tubes (PMTs) and then by a 16-bit analogue-to-digital (A/D) converter. The sampling is either in analogue and photon-counting modes with a rate of 20 and 800 MHz, respectively, providing 1-minute averaged profiles with vertical resolution of 7.5 m. The full overlap is reached around 250 m for all channels. Due to TONET's configuration, only nighttime measurements were taken during WaLiNeAs campaign. Thus, we have 1-month of available data, around 12 hours per day (6 pm. – 6 am) from 20<sup>th</sup> October to 20<sup>th</sup> November. The WVMR measurements has been calibrated using collocated ground-based meteorological measurements (Chazette et al., 2025).



### TIBIDABO at Barcelona (RL2)

TIBIDABO is a multiwavelength Raman lidar operating at the Barcelona Aerosol Remote Sensing site of ACTRIS (<https://www.actris.eu/>, last access: 28 November 2025). The instrument, which is documented in (Kumar et al., 2011), is installed on the rooftop of the D3 building in the Campus Nord of Universitat Politècnica de Catalunya (UPC), in Barcelona, Spain (41.38° N, 2.11° E; 115 m amsl). This location is in an urban environment, at the bottom of a 500-m altitude mountain range, near the end of the range yielding to the wide Llobregat river valley, at 5 km distance from the sea and 6 km of the Barcelona harbour area. Concerning the water vapor measurements, the system emits 90 mJ at 354.7 nm for a repetition rate of 20 Hz. It uses a 38 cm receiving telescope and detects the returns corresponding to the vibro-rotational Raman scattering of water molecules at 407.5 nm (0.3-nm IF bandwidth), and to the pure-rotational Raman scattering of nitrogen and oxygen at 353.9 nm (0.8-nm IF bandwidth, OD8 at the elastic wavelength and optimized for being temperature independent). Calibrations are performed using daily radiosondes, launched at 500-m distance from the lidar instrument.

### HORUS at Coursan and Grau-du-Roi (RL3 and RL4)

The H<sub>2</sub>O Raman Ultraviolet Sounder (HORUS) (Laly et al., 2024) was installed in Coursan (HORUS-2, 43.23° N 3.06° E, 4 m amsl.) and Le Grau-du-Roi (HORUS-1, 43.52° N 4.13° E, 7 m amsl). Coursan is a town surrounded by lowland landscapes. The river Aude flows through it and there are numerous wetlands. A high proportion of the land is used for agriculture. Le Grau-du-Roi is a south-east-facing coastal site located to the west of the Camargue region. It is bordered by a long sandy beach and surrounded by low-lying terrain. It lies in the southern section of the Rhône delta, where numerous wetlands provide ideal conditions for evaporation.

HORUS lidars have been especially developed for the WaLiNeAs field campaign by Climate and Environmental Sciences Laboratory (LSCE) to measure water vapour profiles in the low troposphere in the framework of WaLiNeAs. HORUS is a new generation of compact, autonomous, eye-safe systems that work with pulsed frequency-tripled Nd:YAG lasers manufactured by Lumibird Quantel. The optical architecture of the HORUS lidar is identical to that of the WALI lidar (described in subsection 2.6). The HORUS-1 model has a pulse energy of 30 mJ at a wavelength of 354.7 nm and a pulse repetition frequency (PRF) of 20 Hz. In contrast, the HORUS-2 model has an PRF of 100 Hz.

Calibration was performed using radiosondes prior and after the field campaign and ground-based meteorological measurements (Laly et al., 2024). The statistical uncertainty is less than 0.3 g kg<sup>-1</sup> for the 1-hour averaged profile below 2 km amsl. with a bias of less than 0.50 g kg<sup>-1</sup>. The HORUS dataset is available as NetCDF files and can be freely downloaded from the AERIS database (<https://doi.org/10.25326/537>, last access: 31 August 2025). Each vertical profile of WVMR is associated with a statistical error profile.

### MARCO at Port-Saint-Louis-du-Rhône (RL5)

The Micro-pulse Atmospheric optical Radar for Climate and weather Observations (MARCO, Di Girolamo et al., 2023b) was deployed at Direction des Services Techniques (Port-Saint-Louis-du-Rhône, 43.39° N, 4.81° E, 5 m amsl). The measurement site is located in a unique environment area, with a quite flat landscape, featuring a mix of freshwater and saltwater ecosystems, with the Rhône River flowing into the Mediterranean Sea. The Raman lidar operated almost continuously over the period from 19 October 2022 to 22 February 2024, collecting approximately 12000 hours of lidar measurements (corresponding to ~ 850 Gshots). MARCO, developed by the University of Basilicata, can operate in all weather conditions, with a 24/7 measurement capabilities, with operation being completely remote-controlled. The system relies on a high-power micro-pulse diode-pumped Nd:YAG laser source emitting pulses at 354.7 nm, with a pulse repetition frequency varying within the interval 10–40 kHz.

During the present field deployment, the laser was operated at a nominal frequency of 20 kHz, with a single pulse energy of 0.25 mJ and an average emitted power of 5 W. The receiver includes a Ritchey–Chrétien telescope (40 cm diameter primary



mirror) and five separate receiving channels including the roto-vibrational Raman backscatter signals from N<sub>2</sub> molecules at 386.7 nm and H<sub>2</sub>O molecules at 407.5 nm. Data acquisition is based on the use of transient recorders, with both analogue and digital sampling capabilities. The lidar is compact and easily transportable, being hosted in a sealed and rugged cabinet  
410 conceived for outdoor operation in all weather conditions, with the following dimensions: 1.35 m × 1.20 m × 1.73 m (W × D × H). The overall small volume (<3 m<sup>3</sup>), weight (750 kg) and power consumption (~900 W) determines a sensitive simplification of the logistics and reduction of costs associated with the transportation and deployment of the system.  
No radiosonde launches were available on site. Hence, for the calibration of the system MARCO, radiosondes from the official  
415 WMO station of Nîmes-Courbessac have been used. The selected radiosonde launches were identified through air trajectory analysis to maximize airmass coincidence with the lidar site. The statistical uncertainty affecting the measurements was assessed through the application of error propagation techniques to photon-counting signals and to the analogue signals converted into pseudo-photon counts (Di Girolamo et al., 2009). For a temporal resolution of 5 min and a vertical resolution of 100 m, the statistical uncertainty affecting night-time water vapor mixing ratio measurements is approximately 0.3-0.4 g kg<sup>-1</sup> up to an altitude of 2 km, but performance degrades during the day. The bias affecting water vapor mixing ratio  
420 measurements, primarily associated with the calibration of these measurements, is estimated to not exceed 0.2 g kg<sup>-1</sup>.

#### **CONCERNING at Toulon (RL6)**

In the frame of the WaLiNeAs campaign, the COmpact RamaN lidar for Atmospheric CO<sub>2</sub> and ThERmodyNamic PROFILING (CONCERNING) was deployed at the University of Toulon (Toulon - La Garde, 43.14° N, 6.01° E, 65 m amsl), where it operated almost continuously over the period from 29 September 2022 to 25 January 2023, collecting approximately 2800  
425 hours of lidar measurements (corresponding to almost 1 G laser shots). The area around the measurement site features a hilly and mountainous terrain, with elevations ranging from sea level to several hundred meters. CONCERNING, designed and developed by the University of Basilicata in cooperation with the Institute of Marine Sciences of the Italian National Research Council and the University of Rome “Sapienza” (Di Girolamo et al., 2023a), provides high-resolution profiles of water vapor mixing ratio extending up to the free troposphere, both in daytime and night-time. It was operated during the field deployment  
430 with a temporal resolution of 10 s and a vertical resolution of 7.5 m. The receiver includes a Newtonian telescope (50 cm diameter primary mirror) and eight detection channels, two of which are the roto-vibrational Raman backscatter signals from N<sub>2</sub> molecules at 386.7 nm and H<sub>2</sub>O molecules at 407.5 nm. CONCERNING uses also rotational Raman channels on O<sub>2</sub> and N<sub>2</sub> molecules. Data acquisition is carried out based on the use of transient recorders, with both an analogue and digital sampling capability. The system is housed in a sealed and rugged cabinet with the following dimensions: 2.60 m × 1.34 m × 2.26 m (W  
435 × D × H).

The calibration was carried out based on comparisons with 8 radiosondes launched from “Ile du Levant” (~20 km South-East) and 10 from the WMO station of Nîmes-Courbessac. Comparisons were restricted to the free troposphere to avoid biases associated with water vapour heterogeneity in the boundary layer. As for the system MARCO, the statistical uncertainty affecting the measurements was calculated through error propagation techniques applied to the photon-counting and analogue signals. For a temporal resolution of 5 min and a vertical resolution of 100 m, the statistical uncertainty affecting water vapor mixing ratio measurements is approximately 0.2 g kg<sup>-1</sup>, valid up to an altitude of 2 km. The bias affecting water vapor, primarily associated with the calibration of these measurements, is estimated to not exceed 0.1 g kg<sup>-1</sup>.  
440

#### **WALI at Cannes (RL7)**

The Water Vapour and Aerosol Lidar (WALI, Chazette et al., 2014b; Totems et al., 2021), embedded in the Mobile Atmospheric Station (MAS) (e.g. Raut & Chazette, 2009), has been installed on the Thales Alenia Space site, close to Cannes (43.54° N, 6.96° E, 4 m amsl). The site is located by the sea. The area is characterised by a swift transition from the  
445



Mediterranean coastline to the rugged hinterland. The peaks generally reach heights between 300 and 600 m. These include Mont Vinaigre (approximately 618 m high) to the west of the site and rocky spurs closer to the seashore at altitudes of just a few hundred metres.

450 The lidar emits an UV pulse energy of  $\sim$ 100 mJ with a repetition rate of 20 Hz at the wavelength of 354.7 nm and fulfils eye-safe conditions. The acquisition was performed for mean profiles of 1000 laser shots leading to a temporal sampling close to 1 minute. The lidar is equipped with six detection channels, which include two channels dedicated to the detection of the water vapor Raman signal at 407.5 nm and the atmospheric nitrogen Raman signal at 386.6 nm (Chazette et al., 2014b). The standard deviation from reference meteorological station is less than  $0.25 \text{ g kg}^{-1}$  and the absolute deviation is less than  $0.4 \text{ g kg}^{-1}$ , with  
455 a calibration coefficient that remains stable over several years (Chazette et al., 2025). For the inter-comparisons, an averaging time of  $\pm 30$  minutes, centred on the time value of the IASI profile, has been considered. As for HORUS, the dataset is available as NetCDF files and can be freely downloaded from the AERIS database (<https://doi.org/10.25326/537>, last access: 31 August 2025). A statistical error profile is provided alongside each WVMR profile.

#### ARTHUS at Ajaccio (RL8)

460 The Atmospheric Raman Temperature and Humidity Sensor (ARTHUS) (Lange et al., 2019) was operated autonomously in Olmeto, Corsica ( $\sim$ 25 km south of Ajaccio airport,  $\sim$ 300 m from the coast, 41.70 N, 8.85 E, 20 m amsl) between 16 September and 10 December 2022. It provides, among other atmospheric variables, high-resolution profiles of WVMR from  $\sim$ 200 m above ground level. The raw-data resolution is selectable and was fixed to a temporal resolution of 10 s and a vertical resolution of 7.5 m during WaLiNeAs. The system emits into the atmosphere only eye-safe laser pulses at the third-harmonic radiation  
465 of a Nd:YAG laser at a wavelength of about 354.8 nm with a repetition rate of 200 Hz and a pulse energy of  $\sim$ 100 mJ. The first- and second-harmonic wavelength of the laser are separated and blocked. Backscattered signals are collected using a Ritchey–Chrétien–Cassegrain telescope with a 40-cm primary mirror. The receiver separated the elastic and three Raman backscatter signals during WaLiNeAs. In addition to WVMR, ARTHUS measures temperature (rotational Raman Channel on O<sub>2</sub> and N<sub>2</sub>), particle backscatter and extinction coefficients simultaneously as well as combined atmospheric variables like  
470 relative humidity or lidar ratio. The four-channel receiver is optimized for high efficiency, strong background suppression, and negligible crosstalk from elastic signals with the Raman signals.

For quality control, the statistical uncertainty of the measured data are derived in real-time with Poisson statistics by using the count rates of the photon-counting data (Behrendt et al., 2002, 2004, 2015, 2020; Wulfmeyer et al., 2016). For even better determination of the uncertainties, their total values are derived with an autocorrelation analysis (Lenschow et al., 2000; Behrendt et al., 2015). This technique also allows for distinguishing between uncorrelated instrumental noise and correlated atmospheric variability, enabling the simultaneous retrieval of total uncertainty profiles and higher-order moments of turbulent atmospheric fluctuations, along with their uncertainties (Behrendt et al., 2015, 2020). For temporal averaging of five minutes and vertical averaging over 100 m, the statistical uncertainties in the measured water vapor mixing ratio are typically smaller than 2% up to altitude of 2 km with the exact value depending on the atmospheric transmission, i.e., the aerosol optical depth  
480 as well as clouds in the laser path (Lange et al., 2019).

**Data availability.** The datasets are published open access on the AERIS database (<https://en.aeris-data.fr/>, last access: 25 November 2025). The IASI products are available at <https://data.eumetsat.int/extended?query=iasi#> (last access: 3 January 2026). The ERA5 products are available at <https://cds.climate.copernicus.eu/datasets> (last access: 3 January 2026).



**Author contributions.** All authors took part in the field campaigns in autumn–winter 2022 and contributed to the data inversion; PC coordinated the field campaign, performed the statistics between lidars, ERA5 and IASI, and wrote the paper. CF coordinated the WaLiNeAs project. AC, PDG, MDP, FL, JT and MS proofread the paper.

490 **Competing interests.** The authors declare that they have no conflict of interest.

**Acknowledgments.** Special thanks to the local authorities of Thales-Alenia-Space, the harbour master of Port Camargue and the Coursan town hall for their welcome during the WaLiNeAs field campaign. The UPC team thanks the technical assistance of Joaquim Giner, Èric Vila and Rubén Tardío. The Spanish groups acknowledge the support of the Ministry for Science and  
495 Innovation to ACTRIS ERIC.

**Financial support.** This research has been supported by the Agence Nationale de la Recherche via the WaLiNeAs project (grant no. ANR-20-CE04-0001). This work was also supported by the French Institut National de l'Univers (INSU) of the Centre National de la Recherche Scientifique (CNRS) and the Commissariat à l'Énergie Atomique et aux Énergies Alternatives  
500 (CEA). Funding was also received from the Horizon Europe Programme (project REALISTIC, grant agreement no. 101086690) and from CNES via the EECLAT and AOS projects. The contribution of the University of Basilicata was also funded by the Italian Ministry for Education, University and Research (grants STAC-UP and Tech4You) and the Italian Space Agency (grant CALIGOLA and PROTEO). The contribution of the Universitat de València has been jointly funded by the Spanish Research Agency's (AEI) through the PELICAN project (PID2021-123881OB-I00) and the Valencia Autonomous  
505 Government through CIAICO2023-088 project. The contribution of the Universitat Politècnica de Catalunya has been partially supported by the Spanish Research Agency's (AEI) RESA-CI (grant no. PID2019-103886RB-I00) and SYRSAC (grant no. PID2023-149747NB-I00) projects, the Catalan Government through AGAUR (grant no. 2021-SGR-1415) and the European Union through Horizon 2020's ACTRIS IMP (grant no. 871115) and ATMO-ACCESS (grant no. 101008004) projects, and Horizon Europe's REALISTIC project (grant no. 101086690).

510 **6 References**

Amato, U., Antoniadis, A., De Feis, I., Masiello, G., Matricardi, M., and Serio, C.: Technical Note: Functional sliced inverse regression to infer temperature, water vapour and ozone from IASI data, *Atmos. Chem. Phys.*, 9, 5321–5330, <https://doi.org/10.5194/acp-9-5321-2009>, 2009.

515 August, T., Klaes, D., Schlüssel, P., Hultberg, T., Crapeau, M., Arriaga, A., O'Carroll, A., Coppens, D., Munro, R., and Calbet, X.: IASI on Metop-A: Operational Level 2 retrievals after five years in orbit, *J. Quant. Spectrosc. Radiat. Transf.*, 113, 1340–1371, <https://doi.org/10.1016/j.jqsrt.2012.02.028>, 2012.

Behrendt, A., Nakamura, T., Onishi, M., Baumgart, R., and Tsuda, T.: Combined Raman lidar for the measurement of atmospheric temperature, water vapor, particle extinction coefficient, and particle backscatter coefficient, *Appl. Opt.*, 41, 7657, <https://doi.org/10.1364/ao.41.007657>, 2002.

520 Behrendt, A., Nakamura, T., and Tsuda, T.: Combined temperature lidar for measurements in the troposphere, stratosphere, and mesosphere, *Appl. Opt.*, 43, 2930–2939, <https://doi.org/10.1364/AO.43.002930>, 2004.

Behrendt, A., Wulfmeyer, V., Hammann, E., Muppa, S. K., and Pal, S.: Profiles of second- to fourth-order moments of turbulent temperature fluctuations in the convective boundary layer: first measurements with rotational Raman lidar, *Atmos. Chem. Phys.*, 15, 5485–5500, <https://doi.org/10.5194/acp-15-5485-2015>, 2015.

525 Behrendt, A., Wulfmeyer, V., Senff, C., Kumar Muppa, S., Späth, F., Lange, Di., Kalthoff, N., and Wieser, A.: Observation of sensible and latent heat flux profiles with lidar, *Atmos. Meas. Tech.*, 13, 3221–3233, <https://doi.org/10.5194/amt-13-3221-2020>, 2020.



530 Blanchet, J., Creutin, J. D., and Blanc, A.: Retreating winter and strengthening autumn Mediterranean influence on extreme precipitation in the Southwestern Alps over the last 60 years, *Environ. Res. Lett.*, 16, 034056, <https://doi.org/10.1088/1748-9326/abb5cd>, 2021.

Boylan, J. W. and Russell, A. G.: PM and light extinction model performance metrics, goals, and criteria for three-dimensional air quality models, *Atmos. Environ.*, 40, 4946–4959, 2006.

Carissimo, A., De Feis, I., and Serio, C.: The physical retrieval methodology for IASI: The  $\delta$ -IASI code, *Environ. Model. Softw.*, 20, 1111–1126, <https://doi.org/10.1016/j.envsoft.2004.07.003>, 2005.

535 Chazette, P., Marnas, F., Totems, J., and Shang, X.: Comparison of IASI water vapor retrieval with H<sub>2</sub>O-Raman lidar in the framework of the Mediterranean HyMeX and ChArMEx programs, *Atmos. Chem. Phys.*, 14, 9583–9596, <https://doi.org/10.5194/acp-14-9583-2014>, 2014a.

Chazette, P., Marnas, F., and Totems, J.: The mobile Water vapor Aerosol Raman LiDAR and its implication in the framework of the HyMeX and ChArMEx programs: application to a dust transport process, *Atmos. Meas. Tech.*, 7, 1629–1647, <https://doi.org/10.5194/amt-7-1629-2014>, 2014b.

540 Chazette, P., Totems, J., and Laly, F.: Long-term evolution of the calibration constant on a mobile/field campaign water vapour Raman lidar, <https://doi.org/10.5194/egusphere-2024-3583>, January 2025.

Clerbaux, C., Chazette, P., Hadji-Lazaro, J., Mégie, G., Müller, J. F., and Clough, S. A.: Remote sensing of CO, CH<sub>4</sub>, and O<sub>3</sub> using a spaceborne nadir-viewing interferometer, *J. Geophys. Res. Atmos.*, 103, 18999–19013, <https://doi.org/10.1029/98JD01422>, 1998.

545 Coopmann, O., Guidard, V., Fourrié, N., Josse, B., and Marécal, V.: Update of Infrared Atmospheric Sounding Interferometer (IASI) channel selection with correlated observation errors for numerical weather prediction (NWP), *Atmos. Meas. Tech.*, 13, 2659–2680, <https://doi.org/10.5194/amt-13-2659-2020>, 2020.

Cuesta, J., Flamant, C., Gaetani, M., Knippertz, P., Fink, A. H., Chazette, P., Eremenko, M., Dufour, G., Di Biagio, C., and Formenti, P.: Three-dimensional pathways of dust over the Sahara during summer 2011 as revealed by new Infrared Atmospheric Sounding Interferometer observations, *Q. J. R. Meteorol. Soc.*, 146, 2731–2755, <https://doi.org/10.1002/qj.3814>, 2020.

EUMETSAT: IASI All Sky Temperature and Humidity Profiles - Climate Data Record Release 1.1 - Metop-A and -B, [https://doi.org/10.15770/EUM\\_SEC\\_CLM\\_0063](https://doi.org/10.15770/EUM_SEC_CLM_0063), 2022.

550 Flamant, C., Chazette, P., Caumont, O., Di Girolamo, P., Behrendt, A., Sicard, M., Totems, J., Lange, D., Fourrié, N., Brousseau, P., Augros, C., Baron, A., Cacciani, M., Comerón, A., De Rosa, B., Ducrocq, V., Genau, P., Labatut, L., Muñoz-Porcar, C., Rodríguez-Gómez, A., Summa, D., Thundathil, R., and Wulfmeyer, V.: A network of water vapor Raman lidars for improving heavy precipitation forecasting in southern France: introducing the WaLiNeAs initiative, *Bull. Atmos. Sci. Technol.*, 2, <https://doi.org/10.1007/s42865-021-00037-6>, 2021.

Fouladi, R. T. and Steiger, J. H.: The fisher transform of the pearson product moment correlation coefficient and its square: Cumulants, moments, and applications, *Commun. Stat. Simul. Comput.*, 37, 928–944, <https://doi.org/10.1080/03610910801943735>, 2008.

555 Fourrié, N., Nuret, M., Brousseau, P., Caumont, O., Doerenbecher, A., Wattrelot, E., Moll, P., Bénichou, H., Puech, D., Bock, O., Bosser, P., Chazette, P., Flamant, C., Di Girolamo, P., Richard, E., and Saïd, F.: The AROME-WMED reanalyses of the first special observation period of the Hydrological cycle in the Mediterranean experiment (HyMeX), *Geosci. Model Dev.*, 12, 2657–2678, <https://doi.org/10.5194/gmd-12-2657-2019>, 2019.

Di Girolamo, P., Summa, D., and Ferretti, R.: Multiparameter Raman lidar measurements for the characterization of a dry stratospheric intrusion event, *J. Atmos. Ocean. Technol.*, 26, 1742–1762, <https://doi.org/10.1175/2009JTECHA1253.1>, 2009.

560 Di Girolamo, P., Dionisi, D., Cacciani, M., Di Bernardino, A., Franco, N., Summa, D., Di Paolantonio, M., Iannarelli, A. M., and Di Iorio, T.: A Compact Raman Lidar for Atmospheric CO<sub>2</sub> and Thermodynamic Profiling: The System CONCERNING, in: *Proceedings of the 30th International Laser Radar Conference*, 531–537, [https://doi.org/10.1007/978-3-031-37818-8\\_69](https://doi.org/10.1007/978-3-031-37818-8_69), 2023a.



575 Di Girolamo, P., Franco, N., Di Paolantonio, M., Summa, D., and Dionisi, D.: Atmospheric Thermodynamic Profiling through the Use of a Micro-Pulse Raman Lidar System: Introducing the Compact Raman Lidar MARCO, Sensors, 23, 8262, <https://doi.org/10.3390/s23198262>, 2023b.

580 Guidard, V., Fourré, N., Brousseau, P., and Rabier, F.: Impact of IASI assimilation at global and convective scales and challenges for the assimilation of cloudy scenes, Q. J. R. Meteorol. Soc., 137, 1975–1987, <https://doi.org/10.1002/qj.928>, 2011.

585 Guinaldo, T., Voldoire, A., Waldman, R., Saux Picart, S., and Roquet, H.: Response of the sea surface temperature to heatwaves during the France 2022 meteorological summer, Ocean Sci., 19, 629–647, <https://doi.org/10.5194/os-19-629-2023>, 2023.

590 Heilliette, S., Rochon, Y. J., Garand, L., and Kaminski, J. W.: Assimilation of infrared radiances in the context of observing system simulation experiments, J. Appl. Meteorol. Climatol., 52, 1031–1045, <https://doi.org/10.1175/JAMC-D-12-0124.1>, 2013.

Held, I. M. and Soden, B. J.: WATER VAPOR FEEDBACK AND GLOBAL WARMING1, Annu. Rev. Energy Environ., 25, 441–475, <https://doi.org/10.1146/annurev.energy.25.1.441>, 2000.

595 Hersbach, H., Bell, B., Berrisford, P., Hirahara, S., Horányi, A., Muñoz-Sabater, J., Nicolas, J., Peubey, C., Radu, R., Schepers, D., Simmons, A., Soci, C., Abdalla, S., Abellán, X., Balsamo, G., Bechtold, P., Biavati, G., Bidlot, J., Bonavita, M., De Chiara, G., Dahlgren, P., Dee, D., Diamantakis, M., Dragani, R., Flemming, J., Forbes, R., Fuentes, M., Geer, A., Haimberger, L., Healy, S., Hogan, R. J., Hólm, E., Janisková, M., Keeley, S., Laloyaux, P., Lopez, P., Lupu, C., Radnoti, G., de Rosnay, P., Rozum, I., Vamborg, F., Villaume, S., and Thépaut, J. N.: The ERA5 global reanalysis, Q. J. R. Meteorol. Soc., 146, 1999–2049, <https://doi.org/10.1002/qj.3803>, 2020.

595 Hilton, F., Atkinson, N. C., English, S. J., and Eyre, J. R.: Assimilation of IASI at the Met Office and assessment of its. Impact through observing system experiments, Q. J. R. Meteorol. Soc., 135, 495–505, <https://doi.org/10.1002/qj.379>, 2009.

600 Hilton, F., Armante, R., August, T., Barnet, C., Bouchard, A., Camy-Peyret, C., Capelle, V., Clarisse, L., Clerbaux, C., Coheur, P.-F., Collard, A., Crevoisier, C., Dufour, G., Edwards, D., Fajjan, F., Fourré, N., Gambacorta, A., Goldberg, M., Guidard, V., Hurtmans, D., Illingworth, S., Jacquinot-Husson, N., Kerzenmacher, T., Klaes, D., Lavanant, L., Masiello, G., Matricardi, M., McNally, A., Newman, S., Pavelin, E., Payan, S., Péquignot, E., Peyridieu, S., Phulpin, T., Remedios, J., Schlüssel, P., Serio, C., Strow, L., Stubenrauch, C., Taylor, J., Tobin, D., Wolf, W., and Zhou, D.: Hyperspectral Earth Observation from IASI: Five Years of Accomplishments, 2012a.

Hilton, F. I., Newman, S. M., and Collard, A. D.: Identification of NWP humidity biases using high-peaking water vapour channels from IASI, Atmos. Sci. Lett., 13, 73–78, <https://doi.org/10.1002/asl.366>, 2012b.

605 IPCC: Climate change 2022: Impacts, Adaptation and Vulnerability. Summary for policymakers. Contribution of Working Group II to the Sixth Assessment Report of the Intergovernmental Panel on Climate Change, in: United Nations Environment Programme UNEP, vol. AR6, Cambridge University Press, 551–712, 2022.

610 Klaes, K. D., Cohen, M., Buhler, Y., Schlüssel, P., Munro, R., Luntama, J.-P., von Engeln, A., Clérigh, E. Ó., Bonekamp, H., Ackermann, J., and Schmetz, J.: An Introduction to the EUMETSAT Polar system, Bull. Am. Meteorol. Soc., 88, 1085–1096, <https://doi.org/10.1175/BAMS-88-7-1085>, 2007.

Kumar, D., Rocadenbosch, F., Sicard, M., Comeron, A., Muñoz, C., Lange, D., Tomás, S., and Gregorio, E.: Six-channel polychromator design and implementation for the UPC elastic/Raman lidar, in: Lidar Technologies, Techniques, and Measurements for Atmospheric Remote Sensing VII, 81820W, <https://doi.org/10.1117/12.896305>, 2011.

615 Laly, F. and Chazette, P.: Comparative analysis of ERA5 and Raman lidar-derived moisture profiles in the framework of the WaLiNeAs field campaigns, Q. J. R. Meteorol. Soc., e5044, <https://doi.org/10.1002/qj.5044>, 2025.

620 Laly, F., Chazette, P., Totems, J., Lagarrigue, J., Forges, L., and Flamant, C.: Water vapor Raman-lidar observations from multiple sites in the framework of WaLiNeAs, Earth Syst. Sci. Data, 16, 5579–5602, <https://doi.org/10.5194/ESSD-16-5579-2024>, 2024.



625 Lange, D., Behrendt, A., and Wulfmeyer, V.: Compact Operational Tropospheric Water Vapor and Temperature Raman Lidar with Turbulence Resolution, *Geophys. Res. Lett.*, 46, 14844–14853, <https://doi.org/10.1029/2019GL085774>, 2019.

630 Lenschow, D. H. H., Wulfmeyer, V., and Senff, C.: Measuring second through fourth-order moments in noisy data, *J. Atmos. Ocean. Technol.*, 17, 1330–1347, [https://doi.org/https://doi.org/10.1175/1520-0426\(2000\)017<1330:MSTFOM>2.0.CO;2](https://doi.org/10.1175/1520-0426(2000)017<1330:MSTFOM>2.0.CO;2), 2000.

635 Masiello, G., Serio, C., Deleporte, T., Herbin, H., Di Girolamo, P., Champollion, C., Behrendt, A., Bosser, P., Bock, O., Wulfmeyer, V., Pommier, M., and Flamant, C.: Comparison of IASI water vapour products over complex terrain with COPS campaign data, *Meteorol. Zeitschrift*, 22, 471–487, <https://doi.org/10.1127/0941-2948/2013/0430>, 2013.

640 Matricardi, M. and McNally, A. P.: The direct assimilation of principal components of IASI spectra in the ECMWF 4D-Var, *Q. J. R. Meteorol. Soc.*, 140, 573–582, <https://doi.org/10.1002/qj.2156>, 2014.

645 Pérez, C., Sicard, M., Jorba, O., Comerón, A., and Baldasano, J. M.: Summertime re-circulations of air pollutants over the north-eastern Iberian coast observed from systematic EARLINET lidar measurements in Barcelona, *Atmos. Environ.*, 38, 3983–4000, <https://doi.org/10.1016/j.atmosenv.2004.04.010>, 2004.

Pougatchev, N., August, T., Calbet, X., Hultberg, T., Oduleye, O., Schlüssel, P., Stiller, B., Germain, K. St., Bingham, G., St Germain, K., and Bingham, G.: IASI temperature and water vapor retrievals - Error assessment and validation, *Atmos. Chem. Phys. Discuss.*, 9, 7971–7989, <https://doi.org/10.5194/acpd-9-7971-2009>, 2009.

650 Randriamiarisoa, H., Chazette, P., Couvert, P., Sanak, J., and Mégie, G.: Relative humidity impact on aerosol parameters in a Paris suburban area, *Atmos. Chem. Phys.*, 6, 1389–1407, <https://doi.org/10.5194/acp-6-1389-2006>, 2006.

655 Ricard, D., Ducrocq, V., and Auger, L.: A climatology of the mesoscale environment associated with heavily precipitating events over a northwestern Mediterranean area, *J. Appl. Meteorol. Climatol.*, 51, 468–488, <https://doi.org/10.1175/JAMC-D-11-017.1>, 2012.

660 Rood, M. J., Covert, D. S., and Larson, T. V.: Hygroscopic properties of atmospheric aerosol in Riverside, California, *Tellus B*, 39, <https://doi.org/10.3402/tellusb.v39i4.15357>, 1987.

665 De Rosa, B., Di Girolamo, P., and Summa, D.: Temperature and water vapour measurements in the framework of the Network for the Detection of Atmospheric Composition Change (NDACC), *Atmos. Meas. Tech.*, 13, 405–427, <https://doi.org/10.5194/AMT-13-405-2020>, 2020.

Schlüssel, P., Hultberg, T. H., Phillips, P. L., August, T., and Calbet, X.: The operational IASI Level 2 processor, in: *Advances in Space Research*, 982–988, <https://doi.org/10.1016/j.asr.2005.03.008>, 2005.

670 Schneider, M., Romero, P. M., Hase, F., Blumenstock, T., Cuevas, E., and Ramos, R.: Continuous quality assessment of atmospheric water vapour measurement techniques: FTIR, Cimel, MFRSR, GPS, and Vaisala RS92, *Atmos. Meas. Tech.*, 3, 323–338, <https://doi.org/10.5194/amt-3-323-2010>, 2010.

675 Tombette, M., Chazette, P., Sportisse, B., and Roustan, Y.: Simulation of aerosol optical properties over Europe with a 3-D size-resolved aerosol model: comparisons with AERONET data, *Atmos. Chem. Phys.*, 8, 7115–7132, <https://doi.org/10.5194/acp-8-7115-2008>, 2008.

680 Wulfmeyer, V., Muppa, S. K., Behrendt, A., Hammann, E., Späth, F., Sorbjan, Z., Turner, D. D., and Hardesty, R. M.: Determination of convective boundary layer entrainment fluxes, dissipation rates, and the molecular destruction of variances: Theoretical description and a strategy for its confirmation with a novel lidar system synergy, *J. Atmos. Sci.*, 73, 667–692, <https://doi.org/10.1175/JAS-D-14-0392.1>, 2016.

685 Xu, D., Liu, Z., Huang, X. Y., Min, J., and Wang, H.: Impact of assimilating IASI radiance observations on forecasts of two tropical cyclones, *Meteorol. Atmos. Phys.*, 122, 1–18, <https://doi.org/10.1007/s00703-013-0276-2>, 2013.

690 Zhou, D. K., Smith, W. L., Larar, A. M., Liu, X., Taylor, J. P., Schlüssel, P., Strow, L. L., and Mango, S. A.: All



weather IASI single field-of-view retrievals: Case study - Validation with JAIVEx data, *Atmos. Chem. Phys.*, 9, 2241–2255, <https://doi.org/10.5194/acp-9-2241-2009>, 2009.